

Tailoring Surface Roughness Using Additive Manufacturing to Improve Internal Cooling

Jacob C. Snyder¹

Mem. ASME

Department of Mechanical Engineering,
Pennsylvania State University,
3127 Research Dr.,
State College, PA 16801
e-mail: Jacob.Snyder2@prattwhitney.com

Karen A. Thole

Mem. ASME

Department of Mechanical Engineering,
Pennsylvania State University,
136 Reber Building,
University Park, PA 16802
e-mail: kthole@engr.psu.edu

Surface roughness present on internal cooling channels produced with additive manufacturing has been previously shown to augment heat transfer and pressure loss to levels similar to traditionally cast turbulators. Given the ability of the surface roughness to improve the cooling performance of small cooling channels, the question arises on whether there is an optimal combination of random roughness features to maximize internal cooling performance. To investigate this question, test coupons with different surface roughness morphologies and magnitudes were manufactured by manipulating the parameters in the laser powder bed fusion additive manufacturing process. The coupons were tested to characterize the friction factor and Nusselt number of the cooling channels over a range of Reynolds numbers. Results showed that certain roughness combinations outperformed others, increasing the internal cooling performance of the channels. Additionally, manipulation of the performance using the process parameters allowed for reductions in build time, which could be useful for controlling component cost.

[DOI: 10.1115/1.4047380]

Keyword: heat transfer and film cooling

Introduction

As metal-based additive manufacturing (AM) technology continues to advance, engineers are increasingly able to tap into the capability of this transformative technology. For the gas turbine industry, advancements in AM technology have enabled advanced repair [1], higher efficiencies through improved combustion [2], rotating hardware [3], and new alloy development [4]. Despite these successes, however, much of the gas turbine industry's use of AM only scratches the surface of what is possible with the technology.

One area of gas turbines for which AM shows much promise is turbine cooling. Advanced cooling is required as turbine inlet temperatures continue to rise with the increasing overall pressure ratios of highly efficient engines. For internal cooling, the goal is to maximize the heat transfer coefficient while minimizing the pressure drop to ensure cooling air is used most efficiently. Many are approaching using AM for convective heat transfer by leveraging the "free" complexity of the process, trying to optimize the design of the cooling geometry. The downside to this approach is ensuring the optimized geometry is produced accurately, as well as accounting for the surface roughness present in the process. To address this downside, the approach of many has been to remove the surface roughness from AM parts. However, previous work by the current authors was some of the first to show that the roughness can be beneficial to internal heat transfer, augmenting the convection [5–7]. Additional work by the current authors has demonstrated the ability to control the surface roughness inside cooling channels using the AM process parameters, thereby impacting the cooling performance [8]. So, while some have taken the approach of leveraging the design space of AM to create optimized geometries for turbine cooling, this study instead seeks to explore the parameter space of AM to maximize the performance of a given geometry through the manufacturing process alone.

The goal of this study was to determine the best combination of AM parameters to generate surfaces that maximize the performance

of a generic microchannel cooling design. The effect of different combinations of additive process parameters on surface characteristics, geometry, pressure drop, and heat transfer is presented and discussed, as are the implications of different parameter choices on manufacturing time.

Review of Literature

Convective heat transfer has been an area of focus for AM literature in recent years. Most of these studies have focused on using the large design space of AM to create novel geometries and configurations, including the use of numerical optimization [9–13].

Equally as important in creating novel geometries is creating novel surfaces. The AM surface roughness itself has been shown to significantly augment internal convective heat transfer [6]. Ventola et al. [14] were the first to show the enhanced heat transfer provided by the roughness on additive surfaces. In their study, the external heat transfer coefficient of additively manufactured fins was determined to be 40% higher than the same smooth geometry. The effect of additive manufacturing roughness on internal convective heat transfer was shown in two studies by Stimpson et al. [6,15], where numerous microchannel designs were tested. These studies, as well as a study by Snyder et al. [5], showed the potential of augmenting convective heat transfer by using additively manufactured microchannels. The augmentation of Nusselt number over a smooth channel for the designs tested was 1.5–3 times, while the augmentation of friction factor was two to eight times, showing that rough additive channels perform in the same regime as many traditional turbulators such as ribs and pin fins.

Given the potential of AM roughness on convective heat transfer, this study seeks a new approach to investigate tailoring the surface roughness to augment internal convection, as opposed to optimize the geometry. This unique approach was first demonstrated by Snyder and Thole [8], where the roughness of AM surfaces was changed by altering the AM process parameters, ultimately impacting the performance of internal and external cooling geometries. For external cooling, changing the AM process parameters improved the overall cooling effectiveness of a shaped cooling hole by 30%. For an internal channel, this same change in parameters resulted in a reduction in friction factor of 50% with only a

¹Corresponding author.

Contributed by the Heat Transfer Division of ASME for publication in the JOURNAL OF TURBOMACHINERY. Manuscript received March 27, 2019; final manuscript received April 18, 2020; published online June 30, 2020. Assoc. Editor: Dr. Jeffrey Bons.

5–10% reduction in heat transfer. Therefore, there is an opportunity to create tailored surface roughness for internal convection through manipulation of the AM process parameters.

The effect of different process parameters on surface roughness has been investigated in literature for select test geometries and materials. Most of these studies have shown that the predominant parameters affecting surface roughness are the parameters that affect the amount of energy input by the laser [16–20]. These include the laser power, laser scanning speed, and laser hatch spacing. For example, Wang et al. [19] showed that a two to three times difference in arithmetic mean roughness (R_a) on the top surface of small cubes could be achieved by varying the laser power, laser speed, and hatch spacing. Specifically, all of these studies saw the same trend where roughness decreased with increasing energy density to a minimum roughness level before increasing again with energy density.

Another key parameter to consider when controlling surface roughness is the use of a contour scan or single laser pass around the edge of each layer. The intent of a contour scan is to re-melt larger roughness features into smaller ones. The general consensus among studies in the literature is that contours are successful in reducing the surface roughness when used correctly [17,21–24]. However, the exact physical phenomena are not well understood. For example, contour parameter changes by Fox et al. [23] failed to generate significant differences in R_a values despite noticeable differences in topography, while contour parameter changes by Koutiri et al. [24] produced two opposing roughness trends for downskin surfaces.

Consequently, the current study seeks to expand upon the work by Snyder and Thole [8] by tailoring the surface roughness within internal cooling channels using different AM process parameters. While AM process parameters have been optimized extensively in the context of material and mechanical properties, the current authors are aware of only one study in the literature that has explored the concept of optimizing process parameters for fluid flow without heat transfer. The study by Fantozzi et al. [25] varied the laser power, scanning speed, and hatch spacing to control the pressure losses through a porous material. However, flow through porous media is significantly different than high Reynolds number turbulent channel flow typically seen in turbine cooling. Additionally, this study by Kinel et al. did not investigate heat transfer. Therefore, the current study is unique in that the thermal performance of an additively manufactured cooling design was optimized through control of the AM process parameters.

Coupon Description

The goal of the current study was to determine the best combination of AM parameters to generate roughness maximizing the performance of a generic microchannel cooling design. To this end, the effect of select combinations of process parameters on surface roughness was first established through the use of test elements. Then, these different parameters were applied to the internal surfaces of cooling channels to establish different surface roughness morphologies and magnitudes. These test coupons were then characterized and tested for flow and heat transfer performance.

The test coupon containing the cooling channels is shown in Fig. 1. This geometry, having 16 rectangular cooling channels, was identical to the L2x geometry previously presented in other studies by the current author [6,8,15]. Geometric parameters for the channels are given in Table 1. The coupons were manufactured with an EOS M280 laser powder bed fusion (L-PBF) machine using Hastelloy-X powder. A build orientation of 45 deg was used as shown in Fig. 1. This orientation established the upskin and downskin surfaces as the two sides of the fins separating the channels. Therefore, each channel has one upskin, one downskin, and two vertical surfaces.

To measure the characteristics of the different surface types used in this study for the coupon microchannels, test elements were also

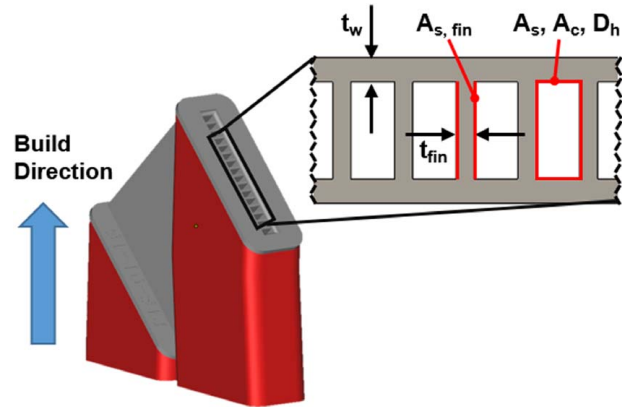


Fig. 1 Diagram of internal cooling test coupon showing build orientation and support material (with callouts). Inset cross section shows the definition of geometric parameters.

Table 1 Geometric parameters for cooling channels

	Nominal value
D_h (mm)	1.26
AR	2.22
S/D_h	1.03
A_c (mm ²)	29.7
L (mm)	25.4
t_w (mm)	0.51
t_{fin} (mm)	0.38

built to characterize the effect of process parameters on surface roughness. These small test elements were designed to emulate a section of the microchannel coupons and built in the same orientation so that the surfaces were representative of the coupons. The test elements were needed to enable destructive inspection of the channel surfaces without damaging the microchannel coupons.

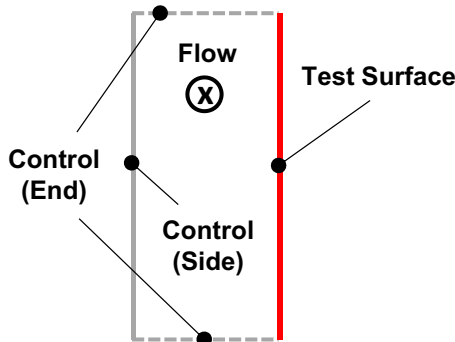
The inspection was performed using scanning electron microscopy (SEM) and optical profilometry (OP). The optical profilometer, a Zyglo Nexview NX2 utilizing coherence inferometry, measured the arithmetic mean height of the surface (S_a) in five discrete locations on the test element channel surfaces. A 10x objective with 0.30 numerical aperture was used for the scanning, producing two-dimensional surface representations with a size of 1.75 mm × 1.75 mm, lateral (x,y) point spacing of 1.6 μm/pixel, and normal (z) resolution of < 1 μm [26,27]. To calculate S_a , a second-order polynomial surface was fit to the data to establish the mean surface while removing large scale curvature. The distance of all of the discrete surface points from this mean surface was then averaged to obtain S_a . This process was repeated for five discrete surface patches to obtain an average S_a value and a 95% confidence. This information is reported on the SEM images and in Table 2.

Study Approach

The approach of this study was to vary the parameters on one wall of channels within the cooling coupon while holding the process parameters with the other three walls of the channel constant. The test surface, as illustrated in Fig. 2, accounted for 35% of the total channel surface area. Three different test surfaces were investigated at two different control levels. A test matrix showing these conditions is given in Table 2. Note that the end surfaces were held constant for all but one of the cases. The characterization of the surfaces and the parameters used to create them are given in the following section. Given the build orientation shown in Fig. 1, the test surface was the upskin, the control-side surface

Table 2 Test coupon matrix showing the use of different surface types and resultant diameter and roughness

Case	Test surface	Control (Side)	Control (End)	$D_{h\text{-meas}}$ (mm)	Area-weighted Channel S_a (μm)	Area-weighted $\frac{S_a}{D_h}$
S-R1-V1	Smooth	Rough 1	Vertical 1	1.26	11.9 ± 0.5	0.0094
R-R1-V1	Rough	Rough 1	Vertical 1	1.38	14.3 ± 1.0	0.0103
B-R1-V1	Ribbed	Rough 1	Vertical 1	1.27	12.2 ± 0.5	0.0096
S-R2-V1	Smooth	Rough 2	Vertical 1	1.23	17.6 ± 1.7	0.0144
R-R2-V2	Rough	Rough 2	Vertical 2	1.30	22.5 ± 4.6	0.0173
B-R2-V1	Ribbed	Rough 2	Vertical 1	1.22	17.9 ± 1.7	0.0147

**Fig. 2 Schematic illustrating the approach of holding 3 of 4 channel surfaces constant (control surfaces) while altering the fourth (test surface)**

was the downskin, and the control-end surfaces were the vertical faces. Also given in Table 2 are the measured hydraulic diameters and area-weighted average S_a values, which will be discussed in the final sub-section of the *Study Approach*.

The approach of varying the test surface only was taken in an attempt to isolate the effect of one particular test surface on the performance of the channel. Since each of the surfaces within an AM part is exposed to different boundary conditions within the build, it is impossible to achieve the same roughness on all surfaces, with the exception of vertically oriented channels [5,28]. Similarly, changing the parameters for the entire channel would result in three different roughness types within the channel due to building direction effects, and it would be impossible to tell which type of roughness was causing the measured change in thermal performance. Therefore, the approach of this study helps to identify the roughness types with the strongest impact on the performance of internal cooling channels.

Development of Roughness-Parameter Relationship. Roughness changes to the surfaces were brought about by changing the laser power, laser scanning speed, hatch distance, and laser scanning strategy, as shown in Table 3. These parameters have been shown to have the largest influence on the surface roughness [16–20]. Each parameter set indicates the laser power (P), and laser scan speed (v) used. For regions with multiple laser passes (hatching), the laser hatch distance is provided. For single laser passes (contours), the beam offset (BO) is provided. Additionally, scaling parameters surface energy flux ($E'' = P/vH_d$) and linear energy density ($E' = P/v$) are given to help to compare simultaneous changes to the process parameters.

For the test surfaces, the three different parameter sets are referred to as “smooth” (S), “rough” (R), and “ribbed” (B). The test surfaces’ resultant from each of these parameter sets is shown in Fig. 3, along with the mean S_a value. For the smooth case, the hatching parameters were chosen to create a small, stable melt

pool during the hatching. This was accomplished by using a low scanning speed and laser power and by using a small hatch spacing. To further reduce the roughness, two consecutive contour passes were utilized to smooth the surface left behind by the hatching step of the process. The surface, shown in Fig. 3(a), was indeed very smooth, with a roughness magnitude (S_a) among the lowest as-manufactured roughness levels that are possible with L-PBF [16–21]. The morphology is characterized by a relatively smooth base surface, with a small amount of partially melted particles on the surface top. This surface was expected to have the smallest impact on the flow through the channels.

The “rough” parameter set was intended to cause a large and irregular surface roughness as shown in Fig. 3(b). To obtain the surface in Fig. 3(b), the laser power, speed, and hatch spacing were all increased from the smooth case. While the surface energy flux was lower than the “smooth” case, the “rough” parameter set created a large melt pool increasing the roughness. Additionally, the high laser power likely caused increased material vaporization, leading to irregular roughness features.

The “ribbed” parameter set was intended to create a different roughness morphology than the other test surfaces as shown in Fig. 3(c). The rib-like morphology of the surface was created by utilizing a higher scanning speed and lower laser power than the smooth case. These parameter changes have been shown to elongate the melt pool, resulting in Plateau-Rayleigh instabilities [29]. With a high length-to-width ratio, the surface tension of the melt pool attempted to break the melt pool into spheres, minimizing its surface energy. This phenomenon caused the non-uniform melt pool cross sections visible in Fig. 3(c). The goal in creating this surface was to create roughness akin to traditional rib turbulators found in many internal turbine passages, but without changing the roughness magnitude from the smooth case. The flow direction was intended to be perpendicular to the ribs.

For the control-side surfaces in Fig. 2, the two levels are referred to as “rough 1” (R1) and “rough 2” (R2). The parameters used to generate these surfaces are presented in Table 3. The goal for these surfaces was to have a “low” roughness level (R1) and a high roughness level (R2). Figure 4 shows the surface resultant from these two parameter sets. The first was the “rough 1” case, shown in Fig. 4(a). This surface was generated using a relatively low energy input for the hatching parameters. Specifically, the parameters were adjusted to target a melt pool penetration depth similar to the layer thickness, which minimized over-melting and prevented large roughness features known as dross. Additionally, the R1 case featured the use of two contours with diminishing energy input to re-melt as much of the roughness as possible. Ultimately, the resultant roughness magnitude was similar to the lowest surface roughness reported for downskin surfaces in this material [21]. The surface morphology of the R1 case is characterized by large roughness features with partially melted particles attached to them. Absent are deep pits and cavities.

The high roughness case (R2) surface, shown in Fig. 4(b), is characterized by extremely large roughness features and a high number of partially melted particles. The S_a value of the R2 case was the

Table 3 L-PBF parameters for different surface types among test coupons

Case	Surfaces	L-PBF Parameters								
		Hatching				Contour 1 / Contour 2				
		P (W)	v (mm/s)	H _d (mm)	E'' (J/mm ²)	P (W)	v (mm/s)	BO (mm)	E' (J/mm)	
S-R1-V1	Test Surface	Smooth	153	600	0.09	2.83	138 / 80	420 / 800	0.012 / 0	0.33 / 0.1
	Control (Side)	Rough 1	145	2400	0.05	1.21	140 / 80	1400 / 1600	0.012 / 0	0.1 / 0.05
	Control (End)	Vertical 1	285	960	0.11	2.70	138 /	420 /	0 /	0.33 /
R-R1-V1	Test Surface	Rough	285	960	0.11	2.70	/ /	/ /	/ /	/ /
	Control (Side)	Rough 1	145	2400	0.05	1.21	140 / 80	1400 / 1600	0.012 / 0	0.1 / 0.05
	Control (End)	Vertical 1	285	960	0.11	2.70	138 /	420 /	0 /	0.33 /
B-R1-V1	Test Surface	Ribbed	153	600	0.09	2.83	88 /	700 /	0 /	0.13 /
	Control (Side)	Rough 1	145	2400	0.05	1.21	140 / 80	1400 / 1600	0.012 / 0	0.1 / 0.05
	Control (End)	Vertical 1	285	960	0.11	2.70	138 /	420 /	0 /	0.33 /
S-R2-V1	Test Surface	Smooth	153	600	0.09	2.83	138 / 80	420 / 800	0.012 / 0	0.33 / 0.1
	Control (Side)	Rough 2	285	960	0.11	2.70	/ /	/ /	/ /	/ /
	Control (End)	Vertical 1	285	960	0.11	2.70	138 /	420 /	0 /	0.33 /
R-R2-V2	Test Surface	Rough	285	960	0.11	2.70	/ /	/ /	/ /	/ /
	Control (Side)	Rough 2	285	960	0.11	2.70	/ /	/ /	/ /	/ /
	Control (End)	Vertical 2	285	960	0.11	2.70	/ /	/ /	/ /	/ /
B-R2-V1	Test Surface	Ribbed	153	600	0.09	2.83	88 /	700 /	0 /	0.13 /
	Control (Side)	Rough 2	285	960	0.11	2.70	/ /	/ /	/ /	/ /
	Control (End)	Vertical 1	285	960	0.11	2.70	138 /	420 /	0 /	0.33 /

largest of all the cases studied. This rough surface was generated by using laser parameters resulting in a high level of energy input that caused the penetration depth of the melt pool to exceed the layer thickness, resulting in large roughness features. Given the many pits and cavities on the surface, it was hypothesized that this roughness morphology would be undesirable for heat transfer. Previous work has hypothesized that porous roughness features that are poorly connected to the base material limit heat transfer performance since the roughness elements do not serve as good heat transfer fins [8,15].

Lastly, the roughness on the control-end surfaces in Fig. 2 was imaged with an optical microscope and is shown in Fig. 5. All test cases but one used the V1 surface for the control-ends, shown in Fig. 5(a). A contour laser pass was used to create a relatively smooth surface by reducing the roughness caused by the basic hatching. On the other hand, the V2 surface shown in Fig. 5(b) has a higher level of roughness because the contour was omitted for this parameter set.

Geometry Characterization. X-ray computed tomography (CT scanning) was used to nondestructively evaluate the six test coupons in this study. Each scan was performed with a voxel size of 29 μm , enabling large scale roughness features to be resolved. The true position of the coupon surface was then determined from the voxel data to within 2.9 μm using a software algorithm. Surface data from the CT scan were then used to calculate several geometric variables of the coupons, as identified in Fig. 1. For the channels, cross-sectional area (A_c) and perimeter (p) were evaluated by processing 850+ image slices along the length of the channels using an in-house code. The values reported for each coupon were averaged across both the length of each channel and the 16 different channels within the coupon. The wetted surface area was determined by multiplying the total average perimeter of all the channels in a given coupon by the channel length. The thickness of the fins (t_{fin}) separating the channels was measured using a software tool designed to measure the local wall thickness of CT data. This tool was applied to a region covering all of the fins to

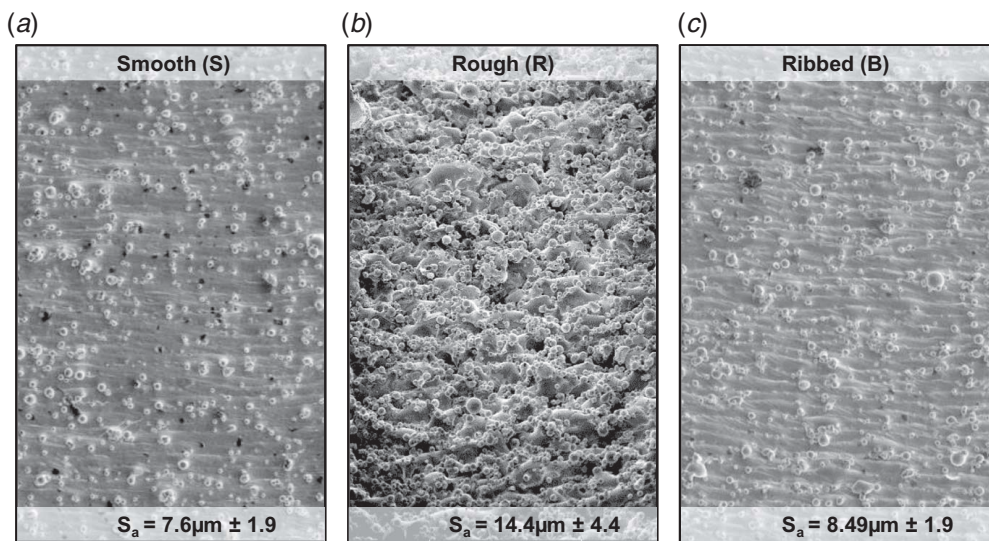


Fig. 3 SEM images showing the test surfaces indicating roughness types: (a) smooth, (b) rough, and (c) ribbed. The width of the images is 1.5 mm.

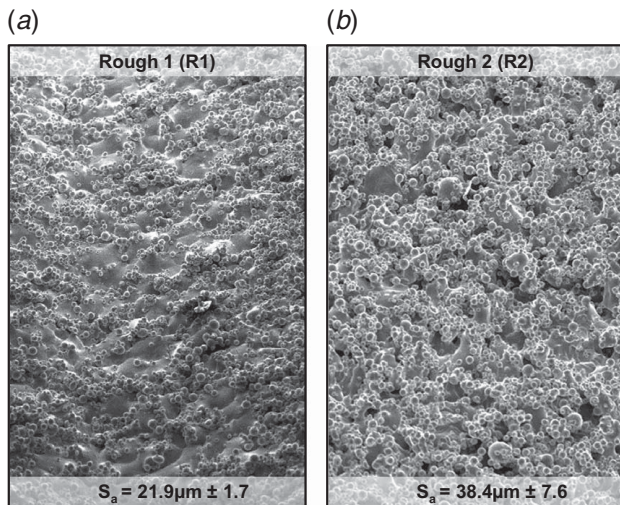


Fig. 4 SEM images showing the different roughness types (a) rough 1 and (b) rough 2 used for the control-side surfaces. The width of images is 1.5 mm.

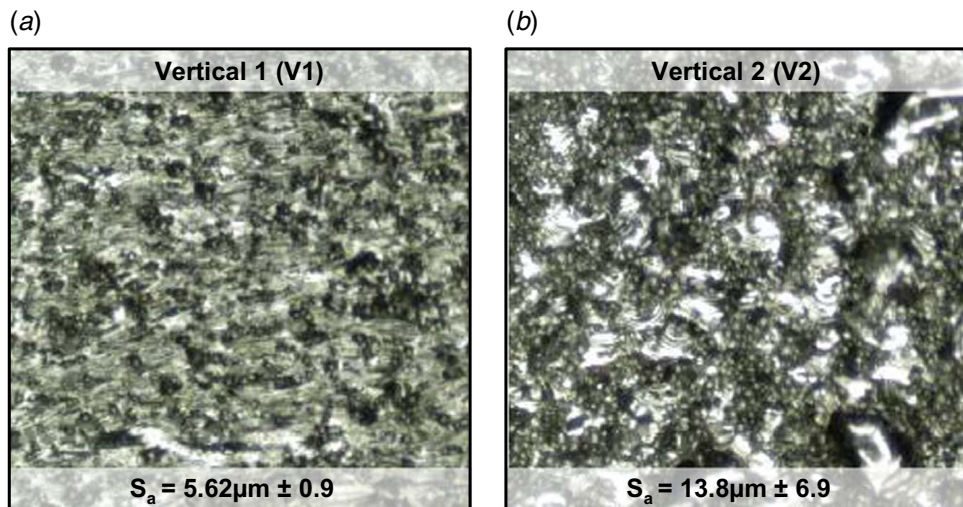


Fig. 5 Optical microscope images of control-end surfaces used in this study showing the (a) V1 and (b) V2 coupons

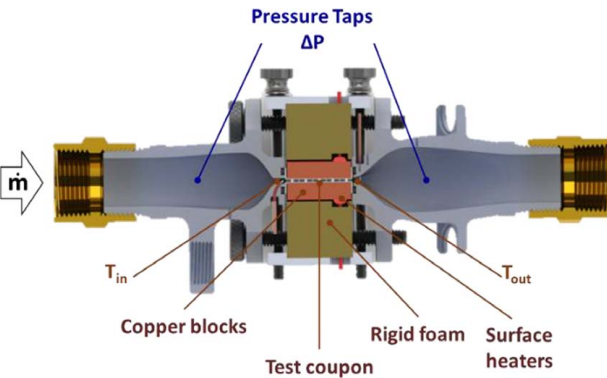


Fig. 6 Section view of the test rig used for pressure loss and heat transfer measurements

For the heat transfer tests, a constant temperature boundary condition was applied to both sides of the coupon using a heater assembly. The assembly consisted of resistance heaters joined to copper blocks via a layer of thermal paste, all encased by rigid foam insulation. To ensure proper thermal contact, a thin layer of thermal paste was also applied between the coupon and copper block surfaces. Multiple thermocouples were located throughout the copper block and rigid foam to determine the copper block temperature and to estimate conduction losses through the foam.

To calculate the heat transfer coefficient, the energy absorbed by the fluid was determined by calculating the electrical power dissipated in the heaters, less the estimated conduction losses. This energy input was verified by also measuring the heat absorbed by the fluid using inlet and exit temperatures. The two measures of energy input were within 10% of each other for all tests. The internal channel wall temperature was calculated using a 1D conduction analysis starting with the copper block temperature and continuing through the coupon using the measured wall thickness from the CT scans. This wall temperature was then used with the fluid inlet and exit temperatures to calculate the log-mean temperature difference. Finally, the heat input to the system, the log-mean temperature difference, and the surface area of the channels measured from the CT scans were used to calculate a bulk heat transfer coefficient using Eq. (2).

$$h = \frac{Q_{in,heater} - \sum Q_{loss}}{A_s \cdot \Delta T_{lm}} \quad (2)$$

Uncertainty was calculated for the friction factor and Nusselt number using the method described by Kline and McClintock [30]. Uncertainty in friction factor ranged from 5% to 20% with the higher uncertainty at the lower Reynolds number; however, the uncertainty was below 8% for all cases with $Re > 7000$ and 5% for $Re > 20,000$. Uncertainty in Nu was 7% for all tests.

Process Parameter Effects on Geometry and Roughness. To investigate the outcome of the channel surfaces, slices of CT scan data are shown in Fig. 7 for three of the test cases. Note that measurements for all of the test coupons were completed, but only three cases are shown to illustrate the effects of the process parameters. Black regions indicate solid material while white regions indicate the open air of the channel in Fig. 7. The left-hand side of the fins is the test surfaces, while the right-hand side of the fins is the control surfaces. Qualitatively, the roughness of the surfaces seen in the CT scan slices agrees with the trends expected—the rough parameter set resulted in rough surfaces, while the smooth parameter set resulted in smooth surfaces. However, the channel cross sections suggest that the changes to parameters affected the geometry of the channels in addition to the roughness. For example, the fins separating the channels in the case with the rough test surface are thinner than the other cases, resulting in a slightly larger channel.



Fig. 7 Slices from CT scans showing channel geometry and roughness. Test surfaces are facing to the left, control-side surfaces facing to the right. Black indicates solid material.

To quantify these differences in the channel geometry, measurements were made of the various geometric parameters identified in Fig. 1. The dimensions measured from the CT data, representing an average of the 16 channels, are shown in Fig. 8 normalized by their respective design intent. As expected from the slices in Fig. 7, the largest deviations from the design intent were seen with the fin thickness (t_{fin}). Specifically, the rough test surface resulted in fin thicknesses over 40% smaller than the design intent. This result may be attributed to the high laser power used for the rough test surface, which was expected to cause some material vaporization, ultimately inhibiting the proper fusion of material in these regions. A side effect of the reduced fin thickness was an increase in hydraulic diameter, particularly when the rough test surface was paired with the R1 control surface. The rough test surface was most effective at increasing the wetted surface area of the fin when paired with both the R1 and R2 control surfaces, as shown in Fig. 8. This result is important from a convective heat transfer perspective, as increasing the wetted surface area increases the overall heat transfer that occurs from that surface.

Shifting the focus to the roughness in the channels, optical profilometry measurements are shown in Fig. 9 for each of the test cases measured on the test elements. The three hatched bars indicate the mean S_a values present on the different walls of the channel, while the solid bar indicates an area-weighted average roughness for the entire channel, as was calculated in Ref. [15]. While these measurements were taken from the test elements instead of the actual coupons, the potential error of this methodology was minimized by two factors. The first was designing the test elements as a sector of the coupon, thereby replicating the boundary conditions of the coupons during the build process. The second factor was placing the parts near the center of the build plate and randomizing their position to minimize position dependencies. Additionally, the validity of the test element roughness data was verified by confirming the trends among the different elements matched the trends of low-resolution CT scan roughness data taken from the coupons.

Figure 9 shows the area-weighted average channel roughness followed the same basic trend as the test surfaces, with the rough test surface causing the highest roughness. Also evident is the larger difference in S_a between the test surface and the control-side surface for the R2 control group. Therefore, the changes to the test surfaces in the R1 control group had a larger impact on the overall roughness than the R2 control group.

Lastly, the results of the roughness analysis and geometry analysis were combined to estimate the relative, area-averaged roughness

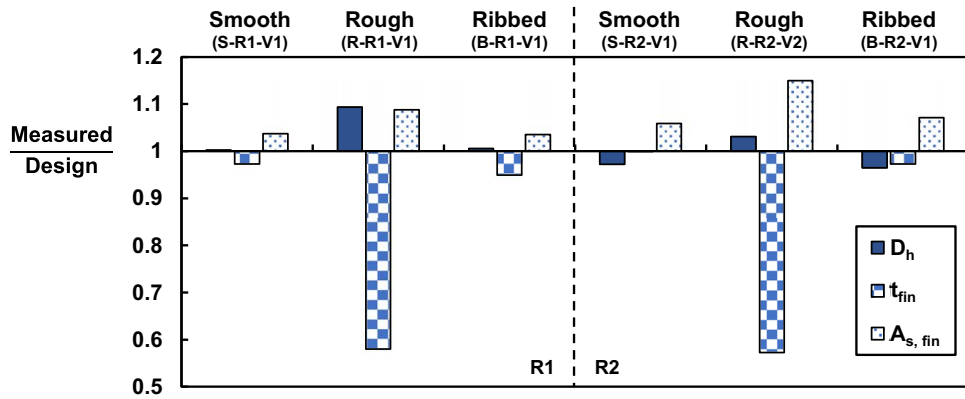


Fig. 8 Measured dimensions from CT scan data normalized by the CAD dimension

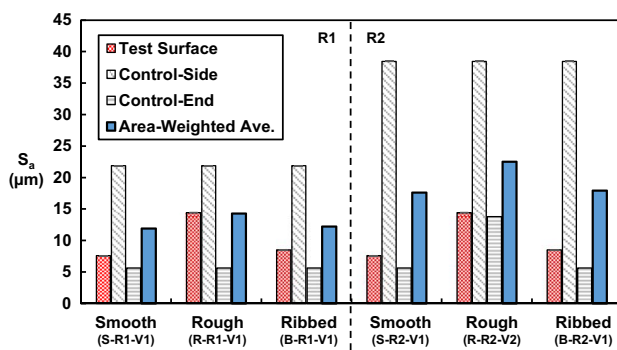


Fig. 9 Optical profilometry data from test elements showing roughness magnitude of different surfaces within cooling channels (hatched) and an area-weighted average roughness for the entire channel (solid)

of the channels for each of the test cases, given in Table 2. As expected, the relative roughness of the cases in the R2 control group was higher than those in the R1 control group. For both control groups, the cases with the smooth and ribbed test surfaces had nearly identical relative roughness. The data also show that the impact of the rough test surface on the overall relative roughness of the channel was reduced by the increase in the hydraulic diameter of these cases.

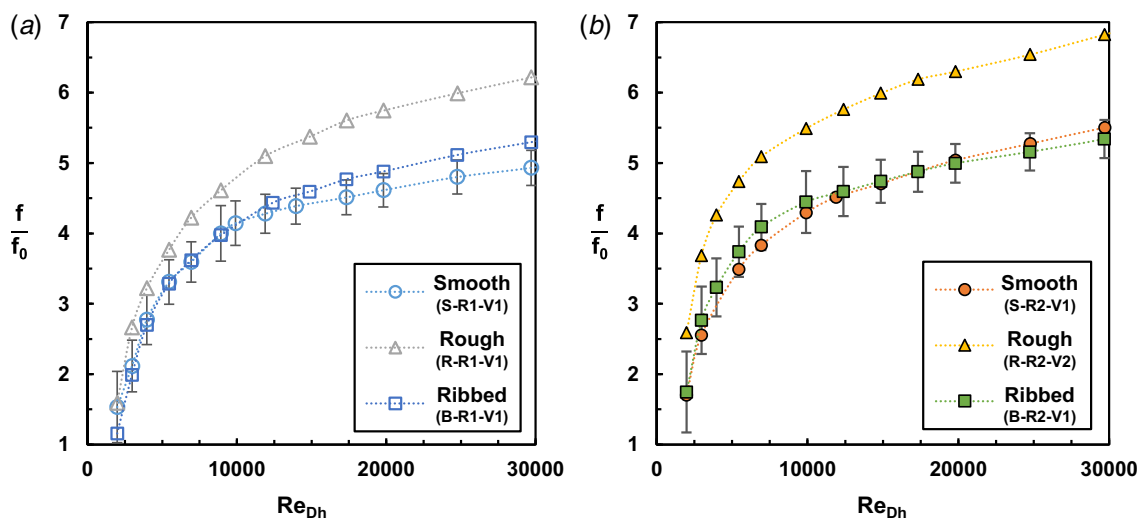


Fig. 10 Friction factor augmentation versus Reynolds number for (a) R1 control surface and (b) R2 control surface

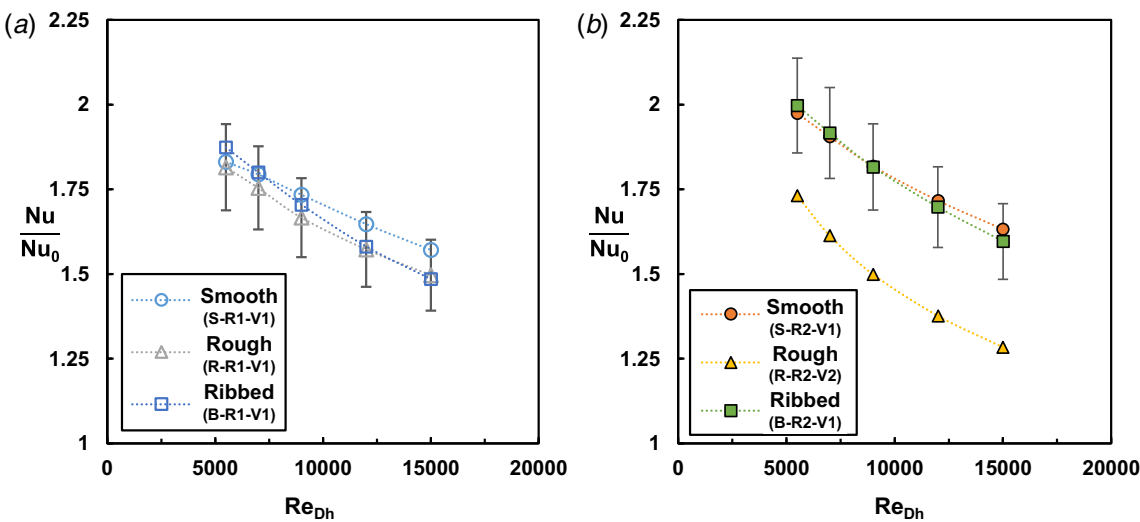


Fig. 11 Nusselt number augmentation versus Reynolds number for (a) R1 control surface and (b) R2 control surface

surface with the R1 control was washed out by the increased roughness of the R2 control. Also shown in Fig. 10(b) is the elevated friction factor of the case with the rough test surface, which had the highest relative roughness of all of the cases shown in Table 2. Recall that this case was roughest overall because the V2 surface was used on the control-end surfaces instead of V1.

The heat transfer performance of these surfaces is shown in Fig. 11 as Nusselt number augmentation versus Reynolds number. Data from the R1 control group, is shown in Fig. 11(a), show little separation among the three test cases—the smooth, rough, and ribbed test surfaces all showed the same heat transfer performance. This result was not expected given the friction trends shown in Fig. 10(a). The case with the rough test surface had a demonstrably higher friction factor than the cases with the smooth and ribbed surfaces, so it was expected that the Nusselt number would also show higher augmentation than the smooth and ribbed cases. This discrepancy is likely attributed to the roughness morphology as originally hypothesized by Stimpson et al. [8,15], whereby the shape of the roughness elements on the rough test surface limited the convective efficiency of the surface.

Figure 11(b) shows that the same trends of the R1 control group were seen with the R2 control group. There was no difference in the heat transfer performance of the smooth and ribbed test surfaces; however, there was a significant difference compared with the rough surface, which showed much lower augmentation. Interestingly, the rough test surface had the highest relative roughness and friction factor but had a noticeably lower Nusselt number than the other cases. The relatively poor heat transfer performance of the cases with the rough test surface was hypothesized to be the result of two factors. The first factor was the poor heat transfer effectiveness of the roughness morphology, as discussed in the previous paragraph. Both the rough test surface and the R2 control surface had roughness morphologies that were expected to have poor heat transfer effectiveness. When combined, these two surfaces limited the overall heat transfer performance of the channel. The second factor contributing to the lower heat transfer was the geometric changes to the fins shown in Figs. 7 and 8. While the parameters for the rough test surface increased the surface roughness of the fin, these parameters also decreased the fin thickness, as quantified in Fig. 8, reducing the fins' ability to conduct heat away from the center of the coupon.

To quantify this effect, the fin efficiency of each test case was calculated and is shown in Fig. 12. The lines represent fin efficiency calculated using the design intent fin thickness, while the symbols denote fin efficiencies calculated using the measured fin thickness

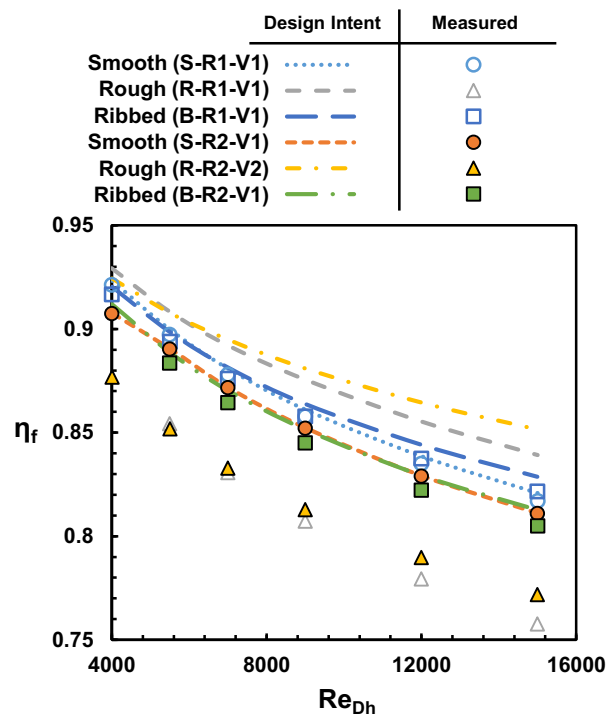


Fig. 12 Fin efficiency calculated using experimental convection coefficient and design dimensions (lines) or average fin thickness measured from CT scan data (symbols) as a function of Reynolds number

from the CT scans. These results confirm that the use of the rough parameter set reduced the fin efficiency of the channel walls. At high Reynolds numbers, the reduction in fin efficiency was around 10% for both cases with the rough test surface.

This decrease in fin efficiency resulting from the change in fin thickness was exaggerated by the fact that the coupons were manufactured with a relatively low thermal conductivity nickel alloy. If the thermal conductivity of the material was increased, either by using a different material or operating at higher temperatures, the fin efficiency would not be as strongly affected by geometric variations to the fins. For example, evaluating the performance of the same Hastelloy-X coupons at an operating temperature of 1000 °C would result in a difference of only 4% between the fin

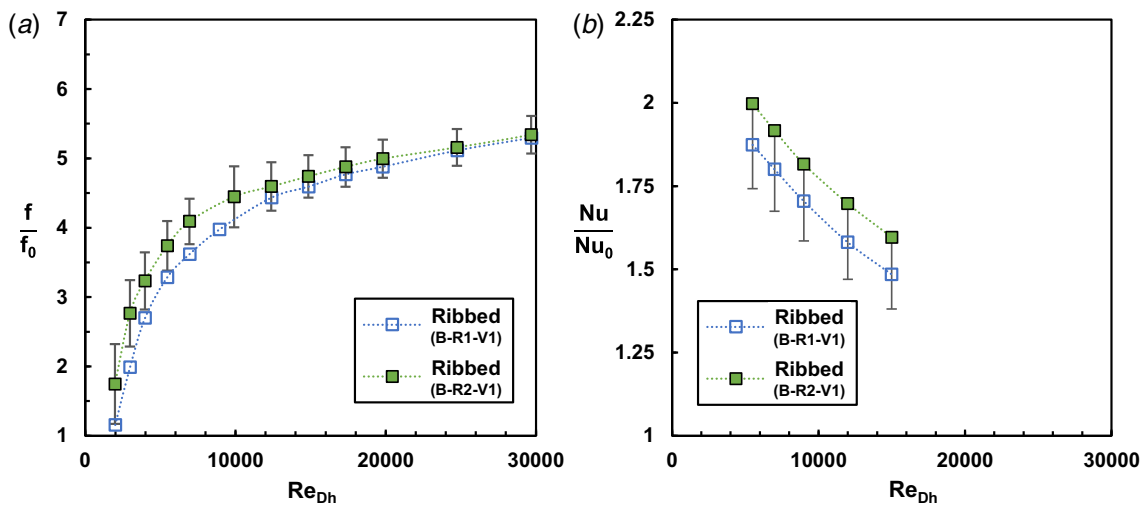


Fig. 13 Augmentation of (a) friction factor and (b) Nusselt number for ribbed test surface under for two different control surfaces

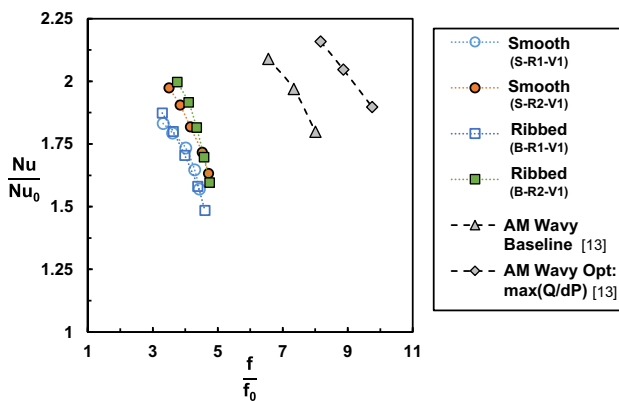


Fig. 14 Nusselt number augmentation versus friction factor augmentation for the cases with smooth and ribbed test surfaces. AM wavy channel data from Kirsch et al. [13] for $\lambda = 0.4L$ case.

efficiency of design geometry versus the thinner measured geometry.

Lastly, the friction and Nusselt number augmentation of the ribbed test surface are compared between the R1 and R2 control surfaces in Fig. 13. The friction was similar between the two cases, but the heat transfer shows a slight increase of around 8% when the ribbed test surface is combined with the R2 control surface instead of R1. This result indicates that there are desirable combinations of roughness morphologies which improve the heat transfer performance of the cooling channels.

To determine which combination of parameters resulted in the best compromise between friction factor augmentation and Nusselt number augmentation, these two values are plotted against each other for the smooth and ribbed test cases and shown in Fig. 14. Overall, the cases where the smooth and ribbed test surfaces were paired with the R2 control surface showed slightly higher Nu and f augmentation than when paired with the R1 control surface. Therefore, a modest improvement to performance was obtained by changing the roughness parameters. Also plotted in Fig. 14 are two sets of data of additively manufactured wavy microchannels from Kirsch and Thole [13]. The optimized dataset represents a design that was numerically optimized from the baseline to maximize heat transfer while minimizing pressure drop. Comparing the performance deltas achieved by tailoring the

surface roughness to the deltas achieved by optimizing the design, altering the roughness was better able to increase the heat transfer while minimizing the impact to friction. However, the magnitude of the changes induced by the roughness changes was smaller than those from the numerical optimization. Kirsch and Thole hypothesized that the inability of the numerical optimization to succeed in achieving the objective function was due to the surface roughness [13]. Therefore, the data from the current study suggest that tailoring the roughness of a simple design to improve performance may be more useful than numerically optimizing a design, if the optimization method does not account for roughness effects.

Comparison to Correlations. The thermal performance of the microchannels was compared with correlations from literature. The correlations proposed by Stimpson et al. [15] for additively manufactured cooling channels were utilized to predict friction factor and Nusselt number for the geometries in this study. For friction factor, the S_a/D_h obtained from the test element roughness was used to calculate the k_s/D_h using the Stimpson's equation, given in Eq. (3). This relative roughness was then used in the Colebrook correlation, given in Eq. (4). Nusselt number predictions were made with the measured friction factor using the correlation proposed by Stimpson, given in Eq. (5).

$$\frac{k_s}{D_h} = 18 \frac{S_a}{D_h} - 0.05 \quad (3)$$

$$\frac{1}{\sqrt{f}} = -2.0 \log \left(\frac{k_s/D_h}{3.72} + \frac{2.51}{Re \sqrt{f}} \right) \quad (4)$$

$$Nu = \frac{\sqrt{f}/8(Re^{0.5} - 29)Pr}{0.6(1 - Pr^{2/3})} \quad (5)$$

For a Reynolds number of 5500, predictions of friction factor were within 10% for all cases except for the smooth and ribbed surfaces from the R2 control group. For a Reynolds number of 12,000, all of the predictions were within 20% of the measured value. Therefore, converting S_a/D_h to k_s/D_h using the scaling proposed by Stimpson et al. [15] works reasonably well to calculate friction factor using the Colebrook equation, although there is some room for improvement.

Predictions of Nusselt number using the measured friction factor and Stimpson's correlation are compared in Fig. 15 at Reynolds numbers of 5500 and 12,000. The results show that the predictions were very close to the measured values. For the low Reynolds

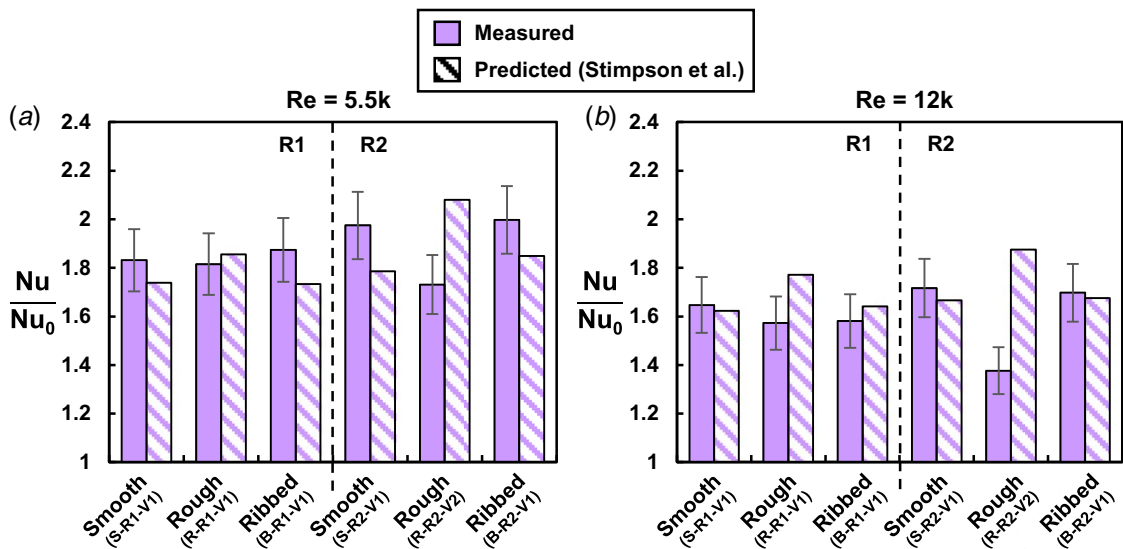


Fig. 15 Measured and predicted Nusselt number augmentation at Reynolds numbers of 5500 (a) and 12,000 (b). Nusselt number predictions were made using the measured friction factor and the correlation proposed by Stimpson [15].

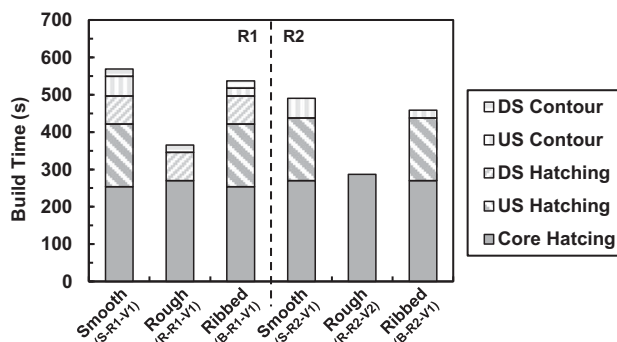


Fig. 16 Estimated build time for each test coupon broken out by time spent in each category of the parameter. Estimates exclude flanges of coupons and do not include miscellaneous delays in the process (for example, recoater passing time).

number, predictions of all cases were within 10% of the measured Nusselt number except for the rough test surface with the R1 control surface. At the high Reynolds number, predictions for were within 4% except for the two cases with the rough test surface. The deviation of the predictions from the measured value for these two cases can be attributed to the reduced fin efficiency of the coupon, as discussed previously.

Overall, if the effect of process parameter changes on roughness is known, the experimental friction factor can be predicted reasonably well from roughness measurements. Moreover, if the experimental friction factor is known, the heat transfer can be well predicted assuming the geometry has not been significantly affected by changes to the process parameters. This result gives further confidence in using the Stimpson correlation to predict the thermal performance of additively manufactured cooling channels.

Manufacturing Considerations. Similarities existed in performance, shown in Fig. 14, between the smooth and ribbed cases when paired with a given control surface. Achieving the same thermal performance using different manufacturing parameters has implications for the build time, and correspondingly, part cost. For example, a simple analysis of the contour speeds shows that switching from the smooth to ribbed parameters would

reduce the amount of time spent on contouring by 40%. Given components designed for convective heat transfer typically have a high surface area to volume ratios, a large portion of the laser scanning time may be dedicated to contouring in these parts. Thus, a 40% reduction in contouring time could have a significant impact on total build time.

To quantify the difference in build time among the different parameters used in this study, an analysis was carried out using the method proposed by Zhang and Bernard [33]. Differences in scanning strategy, hatch spacing, and scanning speed were all captured in this analysis. However, the analysis was performed neglecting the coupon flanges and assuming the parameter changes were only present on the internal channel surfaces. The area of the skin region for each layer was calculated using a skin width of 0.12 mm and an overlap between the skin and core of 0.5 mm to match the settings used for the build.

The results of the analysis, shown in Fig. 16, reveal that for the same thermal performance, switching the parameters for the test surface from smooth to ribbed with the R1 control surface reduced build time by 6%, while a 7% reduction was seen when making the same switch with the R2 control surface. These changes in build time were driven by reductions in contouring time. Alternatively, switching both the test surface and control surface from smooth to ribbed and rough 1 to rough 2, respectively (S-R1-V1 to B-R2-V1) reduced the build time by 19%, while increasing the Nusselt number augmentation by 10–15% for a given friction factor. This reduction in build time was driven by reductions to contour and downskin hatching time. Therefore, parameter selection is extremely important when developing additive components for heat transfer applications. Build time must be taken into account when evaluating the costs and benefits of changes to process parameters targeting increased thermal performance.

Conclusions

In this study, additive manufacturing process parameters were used to systematically control the surface roughness on the internal surfaces of cooling channels. Three test surfaces were investigated: smooth, rough, and ribbed. These different surfaces were created by varying the laser power, scanning speed, hatch distance, and use of contours. Measured results indicated the roughness magnitude changed by a factor of two with these parameter changes.

Geometric analysis of the cooling coupons showed that the parameters used to create the rough test surface caused some deviations in the channel geometry. In particular, the thickness of the fin separating the individual channels was reduced by around 40%. However, the parameters used to create the rough test surfaces were most successful in increasing the wetted surface area of the fins. Friction factor results showed that the rough test surface produced the highest friction factor. There was a slight difference in friction factor between the smooth and ribbed test surfaces when surrounded by relatively smooth channel walls; however, when the roughness of the surrounding channel walls was increased, the differences in friction factor between the smooth and ribbed test surfaces were negligible.

For heat transfer, discrepancies were seen between the relative roughness of the channels and the Nusselt number trends. Specifically, the channels that combined the two roughest surfaces showed the lowest heat transfer performance. This result was due to two factors: the morphology of the rough surfaces limiting the heat transfer effectiveness and a decrease in the fin thickness between channels lowering the fin efficiency.

Intentionally changing the roughness on certain surfaces using the AM process parameters can not only improve the thermal performance of internal cooling channels but also reduce build times and therefore part cost. The optimal parameter combination increased Nusselt number augmentation of 10–15%, while reducing the build time by 19%. Furthermore, when compared with the numerical optimization of wavy microchannels, tailoring the roughness of simple design was better able to increase the heat transfer while minimizing the impact on friction.

Overall, this study has successfully demonstrated the concept of tailoring surface roughness using AM process parameter to improve the performance of a generic microchannel cooling design. This approach illustrates the potential that localized control of the additive process brings to turbine heat transfer. By manipulating the laser parameters in the additive process on certain surfaces, the pressure loss and heat transfer can be affected via the surface roughness alone. This opens the door to optimize the thermal performance along with other metrics like part cost.

Acknowledgment

The authors would like to thank the U.S. Department of Energy National Energy Technology Laboratory for sponsoring research presented in this paper. This paper is based upon work supported by the Department of Energy under Award Number DE-FE0025011.

Disclaimer

This report was prepared as an account of work sponsored by an agency of the United States Government. Neither the United States Government nor any agency thereof, nor any of their employees, makes any warranty, express or implied, or assumes any legal liability or responsibility for the accuracy, completeness, or usefulness of any information, apparatus, product, or process disclosed or represents that its use would not infringe privately owned rights. Reference herein to any specific commercial product, process, or service by trade name, trademark, manufacturer, or otherwise does not necessarily constitute or imply its endorsement, recommendation, or favoring by the United States Government or any agency thereof. The views and opinions of authors expressed herein do not necessarily state or reflect those of the United States Government or any agency thereof.

Nomenclature

f = friction factor

h = convective heat transfer coefficient

k	= thermal conductivity
p	= perimeter
t	= thickness
u	= fluid velocity
v	= laser scanning speed
C	= specific heat capacity
H	= channel height
L	= channel length
P	= static pressure
Q	= heat transfer rate
S	= channel spanwise spacing
T	= static temperature
\dot{m}	= mass flowrate
f_0	= smooth duct friction factor
k_s	= sand-grain roughness
A_c	= cross-sectional area
A_s	= surface area
D_h	= hydraulic diameter
H_d	= laser hatch distance
S_a	= arithmetic mean surface height
E'	= linear energy density
E''	= surface energy density
Nu	= Nusselt number
Nu_0	= smooth duct Nusselt number
Re	= Reynolds number, $u \cdot D_h \cdot \nu^{-1}$

Greek Symbols

Δ	= differential
ε	= sand-grain roughness
η_f	= fin efficiency, $\tanh(m L) \cdot (m L)^{-1}$
ρ	= density
ν	= kinematic viscosity

References

- [1] Andersson, O., Graichen, A., Brodin, H., and Navrotzky, V., 2016, "Developing Additive Manufacturing Technology for Burner Repair," *ASME J. Eng. Gas Turbines Power*, **139**(3), p. 031506.
- [2] Additive Manufacturing Today, 2017, "GE Power Uses 3D Printed Components for Largest and Most Efficient Gas Turbine," Additive Manufacturing Today, <https://additivemanufacturingtoday.com/ge-power-uses-3d-printed-components-for-largest-and-most-efficient-gas-turbine>.
- [3] Siebert, M., 2017, "Breakthrough with 3D Printed Gas Turbine Blades," Siemens AG, Pict. Futur. Mag. Res. Innov.
- [4] Day, D., Kawecki, E., McNally, J. R., and Rosenbarger, T. J., 2018, "Development and Material Characterization of an Additively Manufactured Nickel Alloy for Turbine Applications," ASME Turbo Expo 2018: Turbomachinery Technical Conference and Exposition, Oslo, Norway.
- [5] Snyder, J. C., Stimpson, C. K., Thole, K. A., and Mongillo, D., 2016, "Build Direction Effects on Additively Manufactured Channels," *ASME J. Turbomach.*, **138**(5), pp. 1–8.
- [6] Stimpson, C. K., Snyder, J. C., Thole, K. A., and Mongillo, D., 2016, "Roughness Effects on Flow and Heat Transfer for Additively Manufactured Channels," *ASME J. Turbomach.*, **138**(5), p. 051008.
- [7] Stimpson, C. K., Snyder, J. C., Thole, K. A., and Mongillo, D., 2018, "Effectiveness Measurements of Additively Manufactured Film Cooling Holes," *ASME J. Turbomach.*, **140**(1), p. 011009.
- [8] Snyder, J. C., and Thole, K. A., 2020, "Effect of Additive Manufacturing Process Parameters on Turbine Cooling," *ASME J. Turbomach.*, **142**(5), p. 051007.
- [9] Ferster, K. K., Kirsch, K. L., and Thole, K. A., 2018, "Effects of Geometry, Spacing, and Number of Pin Fins in Additively Manufactured Microchannel Pin Fin Arrays," *ASME J. Turbomach.*, **140**(1), p. 011007.
- [10] Kirsch, K. L., and Thole, K. A., 2017, "Heat Transfer and Pressure Loss Measurements in Additively Manufactured Wavy Microchannels," *ASME J. Turbomach.*, **139**(1), p. 011007.
- [11] Collins, I. L., Weibel, J. A., Pan, L., and Garmella, S. V., 2019, "A Permeable-Membrane Microchannel Heat Sink Made by Additive Manufacturing," *Int. J. Heat Mass Transfer*, **131**, pp. 1174–1183.
- [12] Dede, E. M. M., Joshi, S. N., and Zhou, F., 2015, "Topology Optimization, Additive Layer Manufacturing, and Experimental Testing of an Air-Cooled Heat Sink," *ASME J. Mech. Des.*, **137**(11), p. 111403.
- [13] Kirsch, K. L., and Thole, K. A., 2018, "Experimental Investigation of Numerically Optimized Wavy Microchannels Created Through Additive Manufacturing," *ASME J. Turbomach.*, **140**(2), p. 021002.
- [14] Ventola, L., Robotti, F., Dialameh, M., Calignano, F., Manfredi, D., Chiavazzo, E., and Asinari, P., 2014, "International Journal of Heat and Mass Transfer Rough Surfaces with Enhanced Heat Transfer for Electronics Cooling by Direct Metal Laser Sintering," *Int. J. Heat Mass Transfer*, **75**, pp. 58–74.

- [15] Stimpson, C. K., Snyder, J. C., Thole, K. A., and Mongillo, D., 2017, "Scaling Roughness Effects on Pressure Loss and Heat Transfer of Additively Manufactured Channels," *ASME J. Turbomach.*, **139**(2), p. 021003.
- [16] Spierings, A. B. B., Herres, N., Levy, G., and Authors, F., 2011, "Influence of the Particle Size Distribution on Surface Quality and Mechanical Properties in AM Steel Parts," *Rapid Prototyp. J.*, **17**(3), pp. 195–202.
- [17] Yang, T., Liu, T., Liao, W., Macdonald, E., Wei, H., and Chen, X., 2019, "The Influence of Process Parameters on Vertical Surface Roughness of the AlSi10Mg Parts Fabricated by Selective Laser Melting," *J. Mater. Process. Tech.*, **266**(Sept), pp. 26–36.
- [18] Casalino, G., Campanelli, S. L., Contuzzi, N., and Ludovico, A. D., 2015, "Experimental Investigation and Statistical Optimisation of the Selective Laser Melting Process of a Maraging Steel," *Opt. Laser Technol.*, **65**, pp. 151–158.
- [19] Wang, D., Liu, Y., Yang, Y., and Xiao, D., 2016, "Theoretical and Experimental Study on Surface Roughness of 316L Stainless Steel Metal Parts Obtained Through Selective Laser Melting," *Rapid Prototyp. J.*, **22**(4), pp. 706–716.
- [20] Liu, B., Wildman, R., Tuck, C., Ashcroft, I., and Hague, R., 2011, "Investigation the Effect of Particle Size Distribution on Processing Parameters Optimisation in Selective Laser Melting Process," Proceedings of the Annual International Solid Freeform Fabrication Symposium, University of Texas at Austin, Austin, pp. 227–238.
- [21] Tian, Y., Tomus, D., Rometsch, P., and Wu, X., 2016, "Influences of Processing Parameters on Surface Roughness of Hastelloy X Produced by Selective Laser Melting," *Addit. Manuf.*, **13**, pp. 103–112.
- [22] Ahn, I. H., Moon, S. K., Bi, G., and Wei, J., 2016, "Influence of the Geometric Factor for the Width of the Contour Scan in Selective Laser Melting," Proceedings of the 2nd International Conference on Progress in Additive Manufacturing, pp. 212–215.
- [23] Fox, J. C., Moylan, S. P., and Lane, B. M., 2016, "Effect of Process Parameters on the Surface Roughness of Overhanging Structures in Laser Powder Bed Fusion Additive Manufacturing," *Proc. CIRP*, **45**, pp. 131–134.
- [24] Koutiri, I., Pessard, E., Peyre, P., Amlou, O., and De Terris, T., 2018, "Influence of SLM Process Parameters on the Surface Finish, Porosity Rate and Fatigue Behavior of as-Built Inconel 625 Parts," *J. Mater. Process. Tech.*, **255**, pp. 536–546.
- [25] Fantozzi, G., Kinell, M., Carrera, S. R., Nilsson, J., and Kuesters, Y., 2019, "Experimental Study on Pressure Losses in Porous Materials," *ASME J. Eng. Gas Turbines Power*, **141**(2), p. 021037.
- [26] 2018, "Zygo Nexview NX2 Technical Specifications."
- [27] 2018, "Nexview NX2 / NewView 9000 / ZeGage Pro Objective Chart."
- [28] Snyder, J. C., Stimpson, C. K., Thole, K. A., and Mongillo, D. J., 2016, "Build Direction Effects on Microchannel Tolerance and Surface Roughness," *ASME J. Mech. Des.*, **137**(11), p. 111714.
- [29] Kruth, J., Levy, G., Klocke, F., and Childs, T. H. C., 2007, "Consolidation Phenomena in Laser and Powder-Bed Based Layered Manufacturing," *CIRP Ann.*, **56**(1), pp. 730–759.
- [30] Kline, S. J., and McClintock, F. A., 1953, "Describing Uncertainties in Single-Sample Experiments," *Mech. Eng.*, **75**(1), pp. 3–8.
- [31] Blasius, H., 1913, "Das Aehnlichkeitsgesetz Bei Reibungsvorgängen in Flüssigkeiten," *Mitteilungen Über Forschungsarbeiten Auf Dem Gebiete Des Ingenieurwesens*, Springer, New York, pp. 1–41.
- [32] Gnielinski, V., 1976, "New Equations for Heat and Mass Transfer in Turbulent Pipe and Channel Flow," *Int. Chem. Eng.*, **16**(2), pp. 359–368.
- [33] Zhang, Y., and Bernard, A., 2013, "Generic Build Time Estimation Model for Parts Produced by SLS," High Value Manufacturing: Advanced Research in Virtual and Rapid Prototyping. Proceedings of the 6th International Conference on Advanced Research in Virtual and Rapid Prototyping, pp. 43–48.